2020

Fracture Toughness of Fly Ash-Based Geopolymer Gels: Evaluations Using Nanoindentation Experiment and Molecular Dynamics Simulation

Gideon A. Lyngdoh

Sumeru Nayak

N. M. Anoop Krishnan

Sumanta Das

Fracture toughness of fly ash-based geopolymer gels: Evaluations using nanoindentation experiment and molecular dynamics simulation

Gideon A. Lyngdoh [a], Sumeru Nayak [a], N.M. Anoop Krishnan [b,c,*], Sumanta Das [a,*]

[a] Department of Civil and Environmental Engineering, University of Rhode Island, Kingston, RI, USA
[b] Department of Civil Engineering, Indian Institute of Technology Delhi, Hauz Khas, New Delhi 110016, India
[c] Department of Materials Science and Engineering, Indian Institute of Technology Delhi, Hauz Khas, New Delhi 110016, India

HIGHLIGHTS

- NASH gel is formed through alkaline activation of fly-ash.
- Fracture toughness of NASH gel is obtained from nanoindentation by energy approach.
- Atomistic simulation of N-A-S-H fracture is performed by molecular dynamics.
- Fracture toughness from MD simulation shows good correlation with experimental value.

Keywords:
Fly ash
Geopolymer
Sodium aluminosilicate hydrate gel
Fracture toughness
Nanoindentation
Molecular dynamics
Reactive force field

ABSTRACT

This paper presents the fracture toughness of sodium aluminosilicate hydrate (N-A-S-H) gel formed through alkaline activation of fly ash. While the fracture toughness of N-A-S-H is obtained experimentally from nanoindentation experiment implementing the principle of conservation of energy, the numerical investigation is performed via reactive force field molecular dynamics. A statistically significant number of indentations are performed on geopolymer paste yielding frequency distribution of Young's modulus. Four distinct peaks are observed in the frequency distribution plot from which the peak corresponding to N-A-S-H was separated using statistical deconvolution technique. The young's modulus of N-A-S-H, thus obtained from statistical deconvolution shows excellent match with the values reported in the literature, thus confirming successful identification of indentations corresponding to N-A-S-H. From the load-penetration depth responses of N-A-S-H, fracture toughness was obtained following the principle of conservation of energy. The experimental fracture toughness shows good correlation with the simulated fracture toughness of N-A-S-H, obtained from reactive force field molecular dynamics. The fracture toughness of N-A-S-H presented in this paper paves the way for multiscale simulation-based design of tougher geopolymer binders.

1. Introduction

Geopolymer binders have been extensively investigated by the research community in the last few decades [1-4] for its improved sustainability credentials when compared with ordinary portland cement (OPC). In the geopolymers, the raw materials such as slag, fly ash, Metakaolin or clay are activated by strong alkaline solutions in order to synthesize a poorly crystallized inorganic gel binder [5]. While supplementary cementitious materials (SCMs) have been used as partial replacement of OPC to boost the sustainable credential of the binder [6-9], the geopolymer binders are completely cement-free. In the case of alkali-activated fly ash, owing to the polymerization and poly-condensation effects, sodium aluminosilicate hydrate gel (N-A-S-H) [10-12] is formed which is analogous to calcium silicate hydrate gel (C-S-H) [13,14] in hardened cement paste and calcium aluminosilicate hydrate (C-A-S-H) gel [13,15] in alkali-activated slag (AAS) geopolymer pastes. However, C-S-H, C-A-S-H and N-A-S-H are distinct from each other in their morphology and behavior. The N-A-S-H gel in fly ash-based geopolymer works as the matrix and serves to bind the undissolved inclusions resulting from the remaining raw materials which also contributes to the strength development in the geopolymer concrete [16]. In addition to the significant environmental benefits [17], geopolymers have been shown to offer

excellent performance in a chemically aggressive environment [18], fire events [17], creep [19]. Pore- and micro-structural characteristics of geopolymers have been studied using techniques such as mercury intrusion porosimetry and synchrotron X-ray tomography [20]. The structural characterization of N-A-S-H gel at atomic and nanoscales has been carried out by spectroscopic techniques such as Infrared (IR) [21] and nuclear magnetic resonance (NMR)[22-24] and other experimental techniques like X-ray diffraction (XRD) [25,26], differential thermal analysis (DTA) [27], scanning electron microscopy (SEM) etc. [5,17,28,29]. However, despite the large array of sustainability-related benefits as well as significant research on geopolymers over the previous three decades, these alternative materials are still not adopted widely in the construction industry. One of the major reasons for this is the lack of reliable performance standards which requires evaluation of the link between the material structure at different length scales and engineering performance prediction. As such, it is necessary to develop tools for optimized material design through multiscale numerical simulation. Such simulations would require intrinsic mechanical properties (such as Young's modulus and fracture toughness) of the primary binding phase (i.e. N-A-S-H) as input. While a few recent studies have evaluated Young's modulus of the gel (N-A-S-H) using statistical nanoindentation technique[12,16,20,30-33], fracture toughness of N-A-S-H is not readily available in the literature so far to the best of our knowledge due to highly heterogenous nature of geopolymer binder. This paper makes a significant stride toward that direction by evaluating fracture toughness of N-A-S-H, for the first time, using nanoindentation experiments as well as molecular dynamics simulation. Thus, this study can serve as a starting point toward multiscale numerical simulation-based material design of geopolymers for enhanced fracture performance.

The N-A-S-H gel is synthesized through sodium hydroxide (NaOH)-activation of fly-ash. While various macroscopic experimental methods for fracture response of quasi-brittle materials using different specimen configurations such as semi-circular bending specimen [34-41], and edge notched disc bend specimen [42-44]. three point bending beam specimen [6,9,45,46], cylindrical specimen (to obtain the mode III fracture toughness) [7,8] etc. are evaluated following contact-based methods (clip gauge controlled close-loop experiments) as well as non-contact digital image correlation (DIC) method [45-51], such experimental techniques are not capable of evaluating fracture response of a specific intrinsic phase (such as N-A-S-H) in a highly heterogenous composite (such as geopolymer paste) containing multiple distinct phases distributed randomly in the microstructure. As such, indentation-based techniques can be adopted to evaluate such responses. Micro-indentation and nano-indentation have been used to obtain fracture toughness of various materials such as epoxy coatings [52], quasi-brittle materials [53-56], thin oxide coatings [55,57], shale rocks [58-60] etc. The fracture characterization of thin films has been demonstrated earlier (see Ref.[61]) using nanoindentation techniques. A micro-indentation study demonstrated radial cracks around indenter with lengths around 100 μm (brought about by Vickers micro-indenter when loaded to 1 kg) [61]. However such method suffers from limitations due to the fact that the direction of crack propagation may not be radial [62]. Another approach was proposed by Chen and Bull [63], where the fracture toughness of thin ceramic coating film is computed based on an energetic approach. Along this line, this paper evaluates the fracture toughness of N-A-S-H gel from nanoindentation experiment implementing the principle of conservation of energy. A similar approach has been successfully applied to assess the fracture toughness in the cement paste using nanoindentation [64-66] and micro-indentation [67]. Since no other direct experimental data on fracture toughness of N-A-S-H is available for evaluation of the efficiency of the energy-based approach, the results are compared with fracture toughness of N-A-S-H gel obtained using reactive force field molecular dynamics (MD). Such fundamental scientific evaluation of fracture toughness of N-A-S-H and its comparison with nanoindentation-based experimental approach is expected to provide valuable insights on the ability of such approaches to obtain realistic fracture toughness of N-A-S-H.

The N-A-S-H structure at the molecular level has been recently studied using MD simulation [10,68-74]. In this study, the molecular structure of N-A-S-H gel is developed by hydrating the sodium aluminosilicate (N-A-S) glass structure using Grand Canonical Monte Carlo (GCMC) method [75]. The inter-atomic interactions are modeled using a reactive force field (ReaxFF) [76], which is parametrized for elements such as Na, Al, Si, O, and H [72]. The experimental nanoindentation-based fracture toughness of N-A-S-H is compared with predicted fracture toughness from MD simulation for fundamental insights and to gain confidence on the reported fracture toughness value which is otherwise very difficult to obtain.

2. Experimental procedure

2.1. Materials and mixture proportions

In this study Fly ash (class F type) is used which conforms to ASTM C618 specifications [77] and it contains (mass %) oxides of Si (58.4%), Al (23.8%), Ca (7.32%), Fe (4.19%), Mg (1.11%), Na (1.43%) and K (1.02%). The particle size distribution of fly ash shown in Fig. 1 is obtained by laser diffraction method (using parameters: refractive index: 1.45, 0.01i; rotation Speed: 30 Rev/min; elevation Speed: 20 mm/s and pressure: 0.3 MPa). For sample preparation, an 8 M NaOH solution is used as an alkaline activator to activate the fly-ash. The primary reaction product formed is N-A-S-H gel, which has also been affirmed in the previous work [4,16,17,19].

The preparation of the sample involved mixing of fly ash (precursor) with an activator solution such that a liquid-to-powder ratio equal of 0.4 by mass is achieved. The liquid-to-powder ratio is selected based on the previous work, which has also shown to yield good workability [20,78]. The process involves continuous addition and mixing of the activator to the fly ash for 4 min in a mixer. The resulting mixtures were molded in 50 mm cubes (for

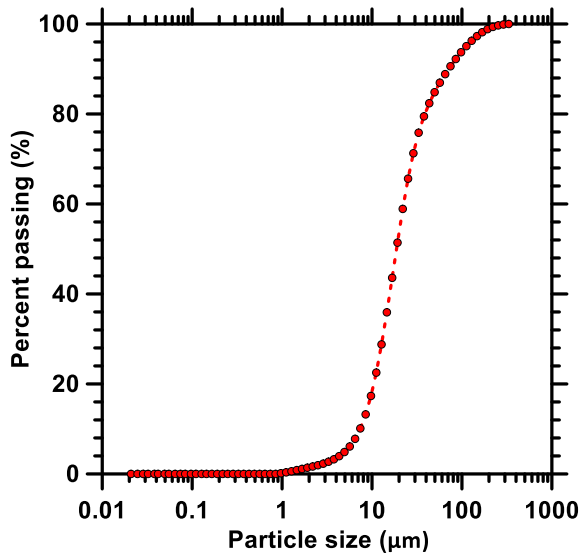

Fig. 1. Particle size distribution of fly ash.

compressive strength evaluation). Samples were also cast in cylindrical molds of size 25 mm diameter and 50 mm length. The molds were then vibrated for 1 min and sealed. The samples were demolded after 24 h and were subjected to heat curing at 75℃ for 48 h in the laboratory oven. After heat curing, the samples were kept in ambient condition for two hours to cool down before performing experiments. No moisture-curing was performed during the sample preparation.

2.2. Compressive strength experiments and mercury intrusion porosimetry

The compressive strengths of cube samples were obtained using Humboldt Compressive machine following ASTM C 109 [79]. Mercury intrusion porosimetry (MIP) was adopted to evaluate the pore characteristics of the fly ash-based geopolymer paste. The MIP experiments were performed using PoreMaster GT mercury intrusion porosimeter by Quantachrome Instruments, United States. The samples for MIP experiments were carved out of the cylinders. The steps adopted for MIP experiments initiate with removal of gases. The sample holder is thereafter filled with mercury thereby raising the pressure to 345 kPa (low pressure). It was followed by high pressure mercury intrusion into the sample. The maximum pressure reached is 414 MPa. Standard properties in the Washburn equation [80-82] to obtain pore diameter include solid–liquid contact angle of 130° and a liquid surface tension of 0.485 N/m.

2.3. Nanoindentation

Prior to the nanoindentation experiment, a 4 mm cube sample was cut using a diamond saw from the core of cylindrical sample (12.5 mm radius and 50 mm length) which was produced following the process explained in section 2.1. Afterwards, a suitable combination of polishing and grinding was adopted for sample preparation. For coarse grinding, the sample is ground by abrasive discs of silicon carbide (SiC) that smoothened the deformations arising from sectioning. A smooth surface is achieved by a 0.04 μm colloidal silica polish. In between polishing stages, ultrasonic cleaning and alcohol rinsing were done to remove the debris from the sample. Such surface preparation techniques resulted in a very smooth surface for SEM and nanoindentation. The sample was left overnight and cured at room temperature. Similar sample preparation method was successfully adopted in previous studies [12,20]. The polished samples were subjected to nanoindentation experiment using a Berkovich tip equipped commercial Nanoindenter (Nano Indenter G200 by Keysight Technologies, United States). A grid size of 10 μm was chosen on a 350 μm × 350 μm area (i.e., 35 × 35 indents) which is considered representative for heterogeneous cementitious systems [25,83]. The indentation locations were judiciously selected prior to testing to avoid pores or cavities during the process. Such technique ensures indentation to take place in solid phases, and it substantially reduces the probability of spurious peaks in the modulus frequency distribution curves. The maximum penetration depth captured in this study is 500 nm. The depth of 500 nm was chosen since it is smaller than the unreacted fly ash inclusions which substantially alleviates phase-interactions [11,14]. The Nano-mechanical characterization of N-A-S-H in the heterogeneous fly ash-based geopolymer was enabled by the statistical nanoindentation technique [20,84,85].

2.4. Method to evaluate the fracture toughness of N-A-S-H from nanoindentation responses

This section explains the method to obtain fracture toughness from load-penetration depth responses utilizing the principle of conservation of energy. The adopted approach involves elastic, plastic, fracture and other negligible energies that sum up to yield the total energy of indentation, according to Equation (1) [63]:

$$W_{tot} = W_{el} + W_{pl} + U_{fr} + U_{other} \tag{1}$$

where $W_{el}$is the work done due to elastic deformation, W_{pl} is the work of pure plastic deformation, U_{fr} is the fracture energy and U_{other} is a work associated with other processes such as heat release (which is neglected here i.e. $U_{other} \rightarrow 0$). The decomposition of energy is illustrated in the schematic diagram of a typical loading–unloading nanoindentation curve (solid line) as shown in Fig. 2.

The total energy (W_{tot}) is defined as the sum of the area under loading curve ($A_1 + A_2$). Here, area A_1 (solid gray) represents combined energy from plastic and fracture portions ($W_{pl} + U_{fr}$) and area A_2 (square shade) represents the elastic energy part (W_{el}) from the unloading curve. Using the same concept, W_{el} can then be computed as the area under the unloading portion of the load-penetration depth curve (Fig. 2); W_{tot} is given by the sum of areas under the whole curve. Having obtained $W_{tot}(A_1 + A_2)$ and $W_{el}(A_2)$ from the corresponding areas under the nanoindentation load-penetration depth curves as explained earlier, the plastic energy can be considered as a function of the residual to total penetration depth as proposed by Cheng et al. (2002). Thus, the plastic energyW_{pl} is calculated as follows [53,63]:

$$W_{pl}/W_{tot} = \frac{2k^2}{1+k} \tag{2}$$

where k is given by (h_f/h_m); h_f denotes the final indentation depth upon complete unloading (residual penetration depth) and h_m denotes the maximum depth of penetration corresponding to maximum load.

Having computed the plastic energy, the other negligible energies are neglected, and the fracture energy can be determined from the balance of total work sans the elastic work and plastic work. Thus, the fracture energy, U_{fr} can be calculated as:

$$U_{fr} = W_{tot} - W_{el} - W_{pl} \tag{3}$$

The fracture toughness is computed from the reduced modulus (E_T) as follows [53,63]:

$$K_c = \sqrt{E_T U_{fr}/A_{fr}} \tag{4}$$

where the term A_{fr} denotes the total interfacial area of the picture frame cracks. Cracks form in the quasi-brittle materials as a result of sharp indentations. The fracture toughness determined from

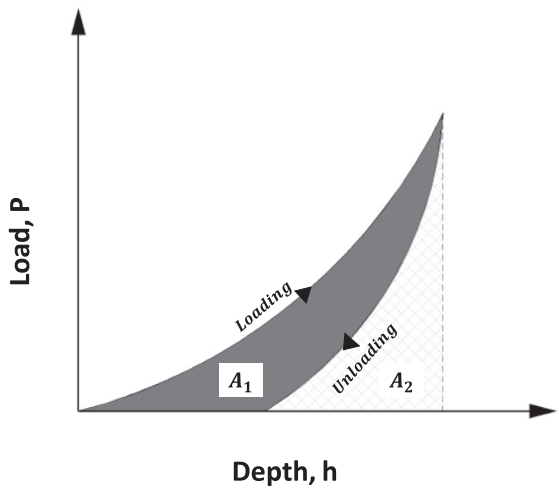

Fig. 2. Nanoindentation P-h curve (solid line) and decomposition of energies (shaded areas) after unloading.

indentation relies on the choice of the indenter geometry and the type of crack formed, e.g., median, radial, half-penny, cone, or lateral cracks [86-88]. In the case of a Berkovich indenter, radial crack morphology (Palmquist) [89] is mainly observed due to the non-symmetrical nature of an indenter. The total length of crack during indentation is given as [90]:

$$c = a + l \tag{5}$$

where '*a*' is the half-diameter of the indented section and 'l' is the length of crack measured from the impression corner. From '*c*', fracture area can be obtained as [90]: $A = \Sigma ct$; where t is the average thickness of the crack. This provides opportunity to obtain fracture toughness from indentation if the crack length is known. However, capturing the extended radial cracking during indentation is challenging in highly heterogenous materials like cementitious binders where multiple phases and random small cracks/pores exist inherently. Besides, such cracks often close after withdrawal of indenter [63]. This is the reason it is extremely challenging, if not impossible, to perform an experimental study for cementitious materials, that tracks the radial cracking around the indenter during indentation process. In the light of such limitations in cementitious binders, the fracture area herein is adopted as: $A = 6at$ (three corners in Berkovich indenter and two surfaces created by each) in absence of direct visual observation of radial cracks during indentation. Here, '*t*' is the thickness of crack (depth of penetration in this case). Besides, the length of radial cracks during indentation in quasi-brittle materials are likely to be very small and hence it is likely that these small radial cracks may not influence the fracture toughness calculation significantly. To evaluate the influence of radial cracks, numerical simulations are also performed which can be found in Section A of the Supplementary document. Furthermore, validity of such adopted approach is evaluated later in this paper by comparison of the obtained fracture toughness of phase corresponding to N-A-S-H with that obtained from experimental studies of fracture toughness of geopolymer paste and mortar since, to the best of our knowledge, direct experimental measurement of fracture toughness for N-A-S-H is not available in the literature. Besides, the scientific viability of the approach is further strengthened in this paper by obtaining fracture toughness of N-A-S-H from MD simulations as explained later in this paper. Such comparative evaluation is expected to shed light on the efficacy of the approach towards obtaining realistic fracture toughness of N-A-S-H.

3. Results and discussions

3.1. Compressive strength and porosity

After heat-curing, the samples were allowed to cool down to ambient temperature. No moist curing was adopted in this study after the heat-curing procedure. The compressive strength of the cubes was determined as per ASTM C 109 [79]. The compressive strength of fly ash-based geopolymer obtained in this study is 28 ± 2.5 MPa from six replicate cube samples. The compressive strength can be further improved by varying the temperature, duration of curing and addition of sodium silicate [91]. Besides, aluminosilicate gel is more likely to continue poly-condensation even after the curing time, and this will further elevate the compressive strength [92]. However, evaluation of fracture toughness of N-A-S-H gel using nanoindentation, being the focus of the study, necessitates formation of an adequate volume of N-A-S-H rather than increasing the compressive strength. The mixture proportion and curing process followed in this paper has been shown to form significant volume of N-A-S-H gel (about 45% of the hardened paste by volume) [12,20]which is sufficient for nano-mechanical evaluation of N-A-S-H gel.

Fig. 3(a) shows the variation of cumulative porosity with the pore diameter and Fig. 3(b) exhibits the pore size distributions, obtained from MIP experiment. Total porosity of 35% is obtained which is in accordance with that reported in [20]. From Fig. 3(b), It is evident that in the fly ash geopolymer binder, small pores with size ranging from 3.6 nm to 2 μm shows dominant contributions towards total porosity. Presence of such sub-micron size pores prevents direct visualization of radial cracks after indentation as mentioned later in this paper.

3.2. Nano-mechanical behavior of N-A-S-H

3.2.1. Evaluation of Young's modulus and identification of N-A-S-H

In the current study, Berkovich tip is used in the nanoindenter to predict the nanomechanical behavior of N-A-S-H phase by continuous stiffness measurement (CSM) technique [93-95]. The CSM technique, unlike the traditional Oliver-Pharr methodology [96], facilitates measurements at any loading point corresponding to any depth of penetration. In the CSM technique, an imposed excitation on the penetrating indenter elicits responses in terms of displacements and phase angles which are recorded continuously. The in-phase and out-of-phase responses are simultaneously resolved to yield the contact stiffness as described in [94]. Practically, the indenter in the nanoindentation experiment is not ideally sharp. Therefore, tip geometry calibration is done by performing a series of indentations on fused silica at various depths of interest. The CSM procedure and relevant calibration process is adequately detailed in[94]. A constant Poisson's ratio of 0.20 is used here since the effect of variation of Poisson's ratio in the range 0.18–0.22 has been reported to be insignificant on the value of calculated Young's modulus [85,97]. For all the indentations, averaged Young's modulus at penetration depth ranging from 100 to 200 nm is determined to avoid surface effects. Thus, from 35 × 35 indentations, statistical distribution of Young's modulus is obtained. The frequency distribution of Young's modulus from all indentations (35 × 35) are shown in Fig. 4(a). In Fig. 4(a) four distinct peaks are observed which can be attributed to four different phases. Similar observations are reported in [20]. In the context of this paper, N-A-S-H is the phase of interest which can be characterized as the first peak (peak corresponding to lowest Young's modulus) in the frequency distribution plot. Statistical deconvolution [84] is performed to obtain mean and corresponding standard deviation for the first peak. The statistical deconvolution procedure is described adequately in [16,98] . In Fig. 4(a), the second peak corresponds to partially activated fly ash, the third peak corresponds to fly ash with cavities/partly activated fly ash and the last peak corresponds to unreacted fly ash. The obtained results are also aligned with a previous study [20]. The Young's modulus, thus obtained for the first peak (16.97 ± 3.8 GPa), correlates very well with the Young's modulus of N-A-S-H reported in the literature [16,20,99] which confirms successful identification of the indentation points that correspond to N-A-S-H. Fig. 4(b) shows variation of Young's modulus for N-A-S-H with varying penetration depth corresponding to a representative indentation point. Average Young's modulus in the penetration depth between 100 and 200 nm is computed. As evident from the plot, the Young's modulus in the penetration depth range of 100–200 nm is invariant of the penetration depth and the surface effects are also avoided when such penetration depth is adopted.

3.2.2. Evaluation of fracture toughness of N-A-S-H

While the indentations points corresponding to N-A-S-H were identified and distinguished from the total dataset in the previous section, this section uses load-penetration depth responses corresponding to those identified indentation points to evaluate the fracture toughness of N-A-S-H following principle of conservation

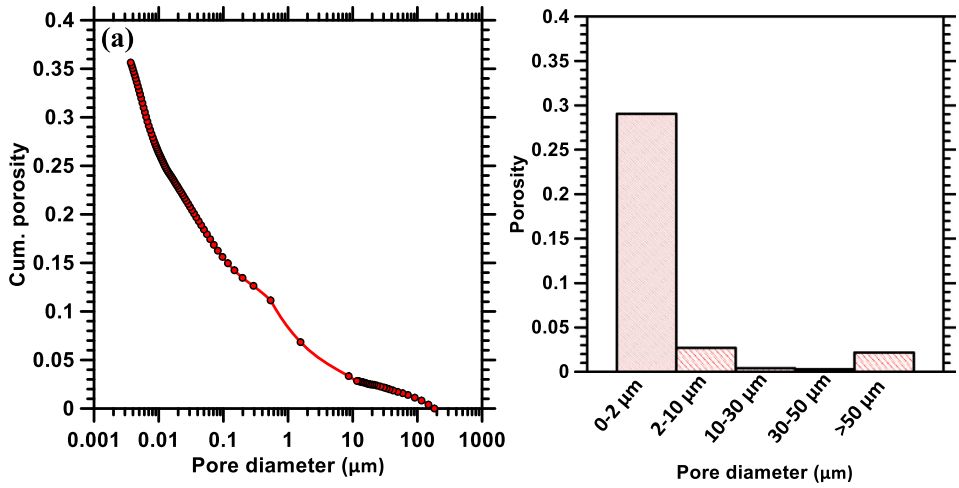

Fig. 3. (a) Cumulative porosity-pore diameter relationship and(b) pore size distribution obtained from MIP experiment.

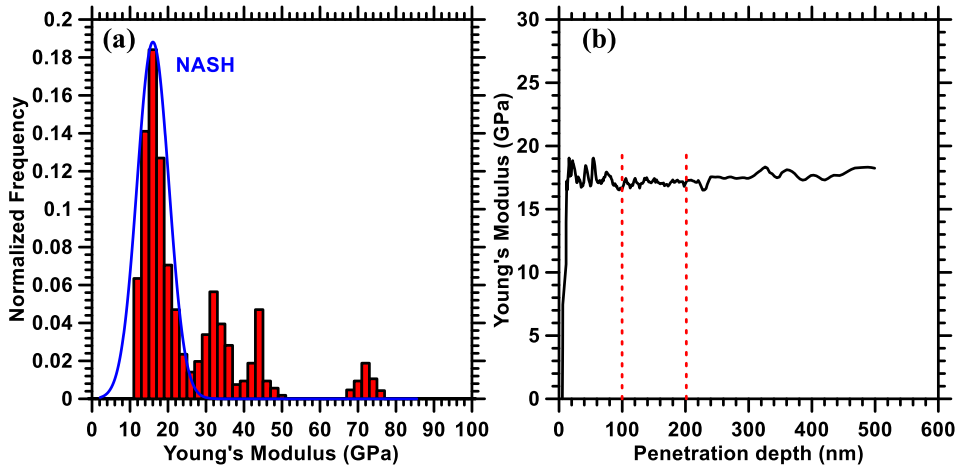

Fig. 4. (a) Histogram showing the distribution of Young's modulus for geopolymer (fly ash-based) with de-convoluted peak for N-A-S-H; (b) Young's modulus with varying depth of penetration for N-A-S-H.

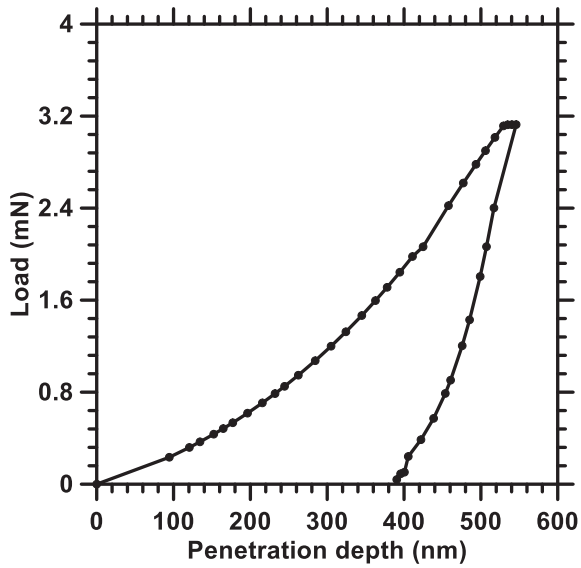

Fig. 5. Representative load-penetration depth response.

of energy as explained in section 2.4. Fig. 5 shows a representative load-penetration depth plot from nanoindentation performed in N-A-S-H. From load-penetration depth responses, the fracture toughness is computed using equation (4) with A_{fr} obtained as 6.81 μm^2. The fracture toughness, thus obtained for N-A-S-H, is 15.18 ± 1.9 MPa-mm$^{0.5}$ (or 0.485 ± 0.06 MPa-m$^{0.5}$).

As noted in the literature [100-103], obtaining the true crack area is crucial in measuring the toughness using nanoindentation techniques. Here, the considered fracture area is less than the actual crack area since it does not consider the radial crack extensions beyond the contact area. To evaluate the influence of such radial crack extensions on the overall fracture area and obtained fracture toughness, an inverse analysis was performed using extended finite element method (please refer to the supplementary document Section A) where the lengths of the radial cracks during indentation were calculated. The analysis revealed that the length of the radial crack extensions is small and, such small radial cracks do not influence the calculated fracture toughness significantly. A difference of about 5% is observed in the obtained fracture toughness if the radial cracks are considered in the fracture area calculation. Hence, in case of nanoindentation experiments on quasi-brittle materials like N-A-S-H using Berkovich indenter, the length of radial crack extensions beyond the contact

area is small and as such, the small radial crack extensions in quasi-brittle materials do not significantly affect the calculation of fracture toughness from indentation.

While experimentally obtained fracture toughness of fly ash-based geopolymer mortar has been reported to be in the range of 0.25–0.47 N-$m^{0.5}$ [104,105], the values in the range of 0.6–0.9 N-$m^{0.5}$ [106] for fracture toughness of geopolymer concrete have been experimentally obtained. Although, we need to keep in mind that geopolymer mortar and concrete are complex heterogeneous systems containing multiple phases such as N-A-S-H, pores, and fly ash in various forms including the unreacted and partially activated phases besides those with cavities, coarse aggregates, fine aggregates and such heterogeneity prevents direct comparison of the aforementioned mortar/concrete results with the obtained fracture toughness of N-A-S-H despite apparent agreement. Hence, in order to evaluate the fundamental scientific viability of the obtained result, the forthcoming section evaluates the fracture toughness of N-A-S-H using reactive force field MD.

3.3. Molecular dynamics simulation to predict the fracture toughness of N-A-S-H

While the previous section evaluated the experimental fracture toughness of N-A-S-H gel, this section focusses on predicting the fracture of N-A-S-H gel using MD simulation. The subsequent sections demonstrate the methodology of N-A-S-H structure preparation, computation of fracture toughness from MD simulation, and results obtained from MD simulation along with a comparison against the experimental value.

3.3.1. Preparation of N-A-S-H structure

The sodium aluminosilicate glass is first prepared by following the melt-quench procedure [10,70,72,107]. The initial structure is constructed by randomly dispersing the Na, Al, Si, and O atoms (approximately 3800 atoms) in the simulation box (35.8 Å × 35.8 Å × 35.8 Å) with a minimum distance of 2 Å between each atom. The glass structure is prepared with Si/Al ratio equal to 2 and Na/Al ratio is kept as unity such that the negative charge caused due to the formation of $[AlO_4]^{-1}$ is neutralized by Na^+ cations. The system is then equilibrated at 4000 K for 500 ps under a canonical (NVT) ensemble. The temperature of the system is then gradually decreased from 4000 K to 300 K in the isothermal isobaric (NPT) ensemble at zero pressure and a rate of 1 K/ps using *NPT* thermostat, ultimately leading to a glass structure at 300 K. This cooling rate has been successfully used to prepare glass structure [108,109]. The obtained structure is then further equilibrated in the NPT (zero pressure) and NVT ensembles, respectively, at 300 K for 500 ps. To obtain the N-A-S-H structure from the glassy structure, a well-established Grand Canonical Monte Carlo (GCMC) simulation [10,72,75,110,111] is implemented using a grand canonical ensemble (μVT) with a chemical potential μ equal to 0 eV to provide unlimited supply of water. The temperature during the GCMC is maintained equal to the system (i.e., 300 K).

In order to reasonably capture the realistic nature of the glass structure and its interaction with water, a reactive force field (ReaxFF) [72] is adopted, along with the charge equilibration method [112] with tolerance of 10^{-6}. Please refer to supplementary material for more details on the reactive force field. The thermodynamic properties are integrated using the Verlet method [113] at a time-step of 0.5 fs. Nose-Hoover [114,115] thermostat is also implemented to control the temperature in the *NPT*. In this study, MD simulation is carried out in an open-source package LAMMPS [116]. The chemical composition for N-A-S glass and N-A-S-H along with water content and density, are shown in Table 1. The computed density from MD simulation from N-A-S-H structure lies in the range from 1.8 to 2.1 g/cm^3, which is in line with the values obtained from experimental observations [70,117-119]. The water content in N-A-S-H lies within the realistic range of 15–20% reported in the literature [117].

To shed more light on the realistic nature of the constructed N-A-S-H structure, the neutron pair distribution function [113,120,121] and structure factor [113,120,121] of the constructed N-A-SH structure is compared with the experimental observations reported in the literature [24,26]. While neutron pair distribution function evaluates the structural characteristics in the short-range order (<3 Å), the structure factor helps to evaluate the medium-range order of the structure (3 Å < r < 10 Å). Fig. 6 (a) and (b) shows the predicted as well as experimental neutron pair distribution function and structure factor respectively. Constructed structure shows good correlation with the experimental data in both and short and medium-range order [23].To quantify the difference between the simulated and experimental total pair distribution function (PDF) g(r), the Wright factor ($\mathscr{R}_x$) is calculated which is expressed as[122]:

$$\mathscr{R}_x = \left[\frac{\sum_{i=1}^{n}(g(r_i) - g_{exp}(r_i))^2}{\sum_{i=1}^{n}(g_{exp}(r_i))^2}\right] \quad (6)$$

where $g_{exp}(r_i)$ is the experimental total PDF. The $\mathscr{R}_x$ value, obtained considering the PDF of the constructed N-A-S-H structure and the experimental data, is 7.8%. It is noted that $\mathscr{R}_x$ value below 12% is considered to be acceptable as explained in the literature [122]. Thus, the quantified $\mathscr{R}_x$ value provides confidence on the validity of the constructed structure of N-A-S-H in the short-range order.

3.3.2. Fracture simulation

In order to simulate the fracture behavior of N-A-S-H gel, a small initial crack is first incorporated in the N-A-S-H structure before applying uniaxial tensile loading. For fracture simulations of N-A-S-H structures, a bounding box of size 143 Å x 143 Å x 35.8 Å (~75000 atoms) is constructed by replicating the bounding box of size 35.8 Å x 35.8 Å x 35.8 Å in the × and y directions. Such a procedure is adopted to reduce the computational demand. Similar procedure has been successfully implemented in the literature [10,14,123]. A pre-existing flaw of size 43 Å x 10 Å x 35.8 Å is incorporated as shown in Fig. 7. The initial crack is constructed by deleting the atoms inside the crack region while maintaining the system charge-neutrality. In this work, a crack/box ratio of 0.30 is maintained in the x-direction. Note that, while crack length can have significant effect on maximum stress achieved for the system, fracture energy is found to be independent of the crack length or system size using the present methodology [124,125]. A detailed analysis of system size and crack length effects has been done by Brochard et al [126] for materials with and without plastic deformations. In the present work, the uniaxial tensile deformation through progressive elongation at a strain rate of 0.001 ps^{-1} (or $10^9 s^{-1}$) is adopted with a time step of 0.5 fs, which is considered to be low enough for atomic restructuring mechanics to takes place in the stressed system, while maintaining computational tractability [68,70]. Similar strain rates are also adopted in MD simulations of similar materials [10,69,127,128]. To ensure that there is no initial stress, an NPT ensemble is used for equilibration. It is observed that the initial crack is maintained after the equilibration, and this ensures that the constructed initial crack is stable. It is to be noted that the crack length can significantly change the maximum stress obtained for the system. However, using the present methodology, crack length or system size has insignificant effects on fracture energy as demonstrated in [125]. Such detailed analysis for both brittle and ductile materials can be found in the literature by Brochard et al [126]. In other words, the fracture energy obtained using the methodology, presented in this paper, has been shown

Table 1
Chemical composition and density of constructed NAS glass and N-A-S-H structures.

Structure	SiO_2(wt %)	Al_2O_3(wt %)	Na_2O (wt %)	Water content(wt %)	Density (g/cm^3)
NAS	59.45	25.22	15.33	0.00	2.45
N-A-S-H	49.37	20.94	12.73	16.95	2.11

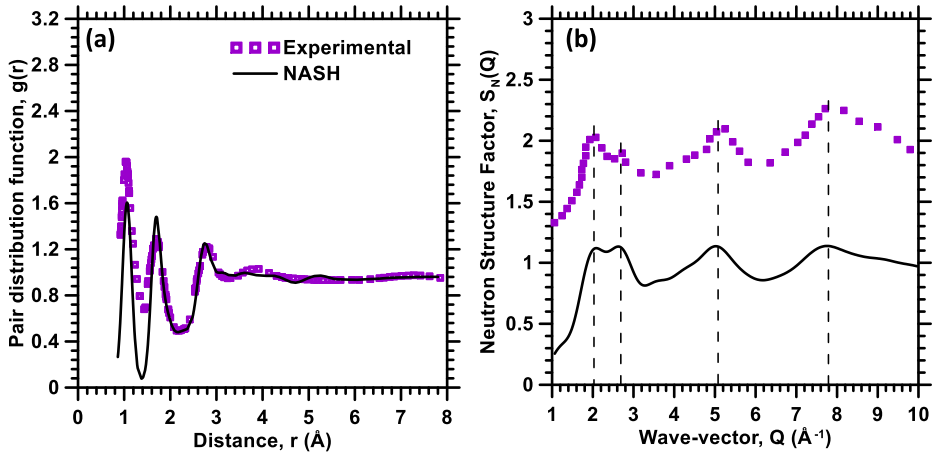

Fig. 6. (a) Pair distribution function and (b) structure factor of the N-A-S-H model, compared with the experimental data.

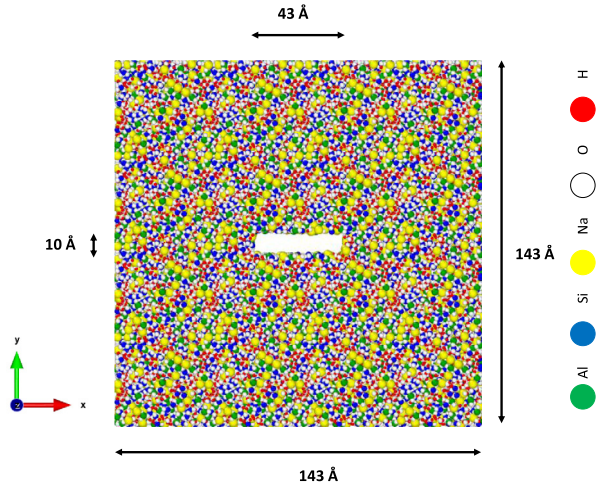

Fig. 7. N-A-S-H structure with initial crack.

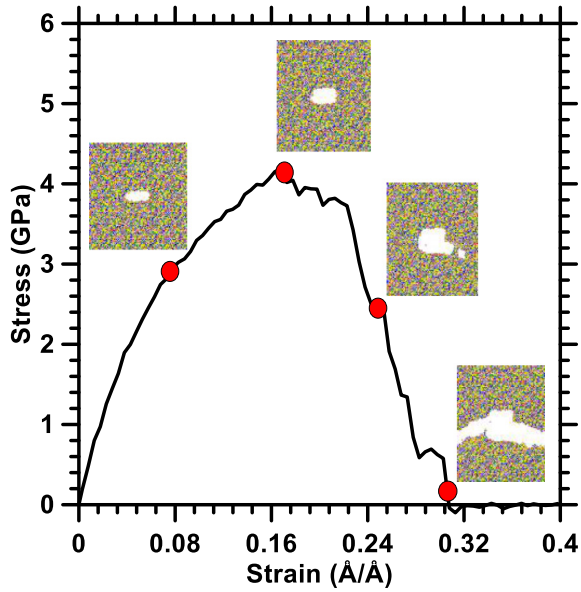

Fig. 8. Tensile stress–strain response of the N-A-S-H structure with initial flaw for 17% water content.

to be insensitive to initial flaw size and box size as shown in [125,126]. To simulate the tensile strain, elongation perpendicular to the initial crack is initiated. The tensile strain is increased until the crack is fully propagated. The entire fracture simulation is performed in the *NVT* ensemble, where the temperature is controlled by a Nose-Hoover thermostat [114,115].

Under applied uniaxial tensile strain, the stress response for the fracture simulation for the N-A-S-H structure is shown in Fig. 8 along with the state of crack propagation at different stages. It is observed that the stress is linearly increased with increasing strain till a strain of approximately 0.08. N-A-S-H structure also shows mild plastic behavior which resists sudden failure of structure after reaching the peak stress. Similar observation is also reported for CSH by Bauchy et al. [14].

To evaluate the fracture properties from MD simulation, the critical strain energy release rate (G_c) is derived based on the energetic theory of fracture mechanism [124,129-131], and the thermodynamics integration is imposed during crack propagation. The advantage of this approach is that no assumption is adopted on the fracture behavior of the material, and hence it is applicable to both brittle [124] and ductile materials [14,132]. In this approach, when the crack is initiated and propagated through the structure, the energy dissipation manifests as fracture energy. The fracture energy is correlated to the critical energy release rate (G_c) which correspond to the energy released per unit area of crack propagated. The expression for critical energy release rate is expressed using thermodynamics integration as [124,126]:

$$G_c = \frac{L_x L_z}{\Delta A} \int_{L_{y0}}^{L_{ymax}} \sigma_y dL_y \tag{7}$$

where $\Delta A = 2L_z\Delta a$; L_z denotes thickness of the bounding box i.e. 35.8 Å, Δa is the length of the crack after it is fully propagated, σ_y is the average stress due to applied uniaxial tensile strain in y direction, and L_x, $L_y$and L_z are the dimension of the bounding box in x, y and z directions respectively. y_0 and y_{max} correspond to the initial dimension along y axis before application of strain and final dimension when the crack is fully propagated, respectively. The above formulation can be directly correlated to the Griffith theory of fracture [129]. To address the plastic deformations and the overlapping of the plastic zones at the periodic boundaries of repetitive unit cells, the fracture area is modified as follows [124]:

$$\Delta A_{eff} = \Delta A - \frac{L_z t r_{pl}}{2} \tag{8}$$

where r_{pl} is the length of plasticity zone which is expressed as follows as per Dugdale-Barenblatt formula[133-135]:

$$r_{pl} = \frac{\pi}{8}\left(\frac{K_{IC}}{\sigma_{pl}}\right)^2 \tag{9}$$

where σ_{pl} is the plastic yield stress of the material. A similar methodology has also been adopted in the literature for silica glass [123,125] and Calcium Silicate Hydrate (CSH) [14]. The relationship between critical stress intensity factor (K_{1C}) and G_c for isotropic materials as per the Irwin's formula [130,136] is given as:

$$K_{1C} = \sqrt{\frac{G_c \times E}{1 - \nu^2}} \tag{10}$$

where E is the Young's modulus of the material, and ν is the Poisson's ratio, obtained from MD simulation of a pristine molecular structure of N-A-S-H. For such simulation, a bounding box size of 143 Å x 143 Å x 35.8 Å was constructed without any preexisting flaw. The bounding box was subjected to uniaxial tensile deformation through progressive elongation at a strain rate of 0.001 ps^{-1} (or $10^9 s^{-1}$) with a time step of 0.5 fs and the tensile stress–strain response was obtained. From the corresponding stress–strain plot, the Young's modulus and Poisson's ratio are computed. For calculation of Young's modulus and Poisson's ratio, the stress–strain response up to a strain of 0.1 is considered which is well within the linear elastic regime. Using the linear regression method, the slope of the stress–strain plot (up to a strain of 0.1) is computed which is adopted as the Young's Modulus of N-A-S-H. On the other hand, the Poisson's ratio is obtained by obtaining the slope from the lateral strain vs longitudinal tensile strain relationship. The Young's modulus and Poisson's ratio, thus obtained from MD simulation, are 20.1 GPa and 0.22 respectfully which correlates well with the experimental values reported earlier in this paper. Similar methodology has been successfully implemented towards MD-based fracture toughness prediction of calcium silicate hydrate (CSH) by Bauchy et al. [14]. It needs to be noted that the precise composition of N-A-S-H, used for experimental evaluation in this study, is not known which makes a direct comparison between the simulated and experimental fracture toughness values of N-A-S-H challenging. While it is certain that alkaline activation of fly ash, as explained in section 2.1, leads to formation of significant amount of N-A-S-H (volume of N-A-S-H was found to be about 45% in the hardened geopolymer paste as obtained using segmentation of a significant number of high resolution SEM images in a previous publication [20]), good correlation between experimental and simulated short-/medium-range order of N-A-S-H (please refer to Fig. 6) indicates realistic nature of constructed molecular structure of N-A-S-H. In addition, the water content in the constructed molecular structure of N-A-S-H lies within the realistic range of 15–20% reported in the literature [117]. Although the exact composition of experimentally formed N-A-S-H is unknown, in the light of the above-mentioned facts, the simulated fracture toughness from MD simulation can be considered comparable to the experimental fracture toughness of N-A-S-H.

Using the aforementioned methodology (Equation (10)), the mode-I fracture toughness of the N-A-S-H gel is obtained as $0.43 MPa.m^{0.5}$, which correlates well with the experimental fracture toughness of 0.485 ± 0.06 MPa-$m^{0.5}$. To further evaluate the fracture response of N-A-S-H, the brittleness/ductility behavior is evaluated by computing the brittleness index (B). The brittleness index is calculated following the procedure detailed in the literature [14], where it is expressed as $B = 2\gamma_s/G_c$. The term γ_s refers to the surface energy. The brittleness index for N-A-S-H is found to be 0.51 which is lower than the value of 0.62 reported for C-S-H [14], suggesting that N-A-S-H structure exhibits more ductility compared to C-S-H in nanoscale.

4. Conclusions

This study presents the evaluation of the fracture toughness of the N-A-S-H gel in fly ash-based geopolymers from the nanoindentation experiment and MD simulations. N-A-S-H gel was synthesized using alkaline activation of fly ash with NaOH. Pore size distribution in the geopolymer paste has been investigated using mercury intrusion porosimetry (MIP). Based on the MIP data, the majority of the pores in size ranges from 0 μm to 2 μm contributes the most to the total porosity. For nanomechanical property evaluation, total 1225 indentations were performed in a 35 × 35 grid from which a frequency distribution plot of Young's modulus was formed. In the frequency distribution plot, four distinct peaks were observed and the first peak with the lowest Young's modulus was identified to belong to N-A-S-H. The following conclusions can be drawn from the study.

- The Young's modulus, obtained from N-A-S-H correlates very well the values reported in the literature which confirms successful identification of indentation points corresponding to N-A-S-H. Based on the principle of conservation of energy, the fracture toughness of N-A-S-H is evaluated from the load-penetration depth response and thus a value of is 0.485 ± 0.06 MPa-$m^{0.5}$ obtained which is found to be in the same order as the fracture toughness of geopolymer mortar and concrete available in the literature.
- To shed more light on the scientific viability of the obtained fracture toughness, fracture toughness of N-A-S-H gel is simulated using reactive force field MD.
- The simulated fracture toughness of N-A-S-H shows an excellent correlation with the experimental value obtained from nanoindentation experiments.
- Such good correlation also reinforces the fact that the radial cracks extending beyond the indenter corners do not significantly influence the fracture toughness of N-A-S-H. Note that the direct observation of radial crack growth during indentation is challenging due to the presence of multiple microcracks and pores of sub-micron size in the heterogenous microstructure of geopolymers. As such, there are significant scopes of improvement for future studies regarding: (i) appropriate estimation of fracture area based on accurate visualization of microcracks during nanoindentation; (ii) consideration of all the possible mechanisms during indentation such as shear flow, local densification etc. and (iii) influence of creep and plasticity at the nanoscale to further bridge the knowledge gaps. Moreover, the fracture toughness of N-A-S-H gel, evaluated here using nanoindentation experiment and MD simulation, can be used as starting point towards multiscale simulation-based design of fly ash-based geopolymers for enhanced performance.

CRediT authorship contribution statement

Gideon A. Lyngdoh: Methodology, Formal analysis, Investigation, Validation, Data curation, Visualization, Writing - original draft. **Sumeru Nayak:** Methodology, Investigation, Data curation. **N.M. Anoop Krishnan:** Methodology, Supervision. **Sumanta Das:** Conceptualization, Methodology, Supervision, Project administration, Resources, Writing - Review & Editing.

Declaration of Competing Interest

The authors declare that they have no known competing financial interests or personal relationships that could have appeared to influence the work reported in this paper.

Acknowledgements

The authors gratefully acknowledge the use of facilities within the Multiscale and Multiphysics Mechanics of Materials Research Laboratory (M4RL) and core research facilities at the University of Rhode Island. Boral Resources is acknowledged for the supply of fly ash. The authors gratefully acknowledge the computing resources provided on the Bluewaves High Performance Research Computing at the University of Rhode Island.

Appendix A. Supplementary data

Supplementary data to this article can be found online at https://doi.org/10.1016/j.conbuildmat.2020.120797.

References

[1] F. Pacheco-Torgal, J. Castro-Gomes, S. Jalali, Alkali-activated binders: A review: Part 1. Historical background, terminology, reaction mechanisms and hydration products, Constr. Build. Mater. 22 (2008) 1305–1314, https://doi.org/10.1016/j.conbuildmat.2007.10.015.

[2] P. Duxson, J.L. Provis, G.C. Lukey, S.W. Mallicoat, W.M. Kriven, J.S.J. van Deventer, Understanding the relationship between geopolymer composition, microstructure and mechanical properties, Colloids Surf., A 269 (2005) 47–58.

[3] P. Duxson, A. Fernández-Jiménez, J.L. Provis, G.C. Lukey, A. Palomo, J.S.J. van Deventer, Geopolymer technology: the current state of the art, J. Mater. Sci. 42 (2007) 2917–2933.

[4] J.L. Provis, S.A. Bernal, Geopolymers and Related Alkali-Activated Materials, Annu. Rev. Mater. Res. 44 (2014) 299–327.

[5] A. Fernández-Jiménez, A. Palomo, Composition and microstructure of alkali activated fly ash binder: Effect of the activator, Cem. Concr. Res. 35 (2005) 1984–1992.

[6] G.L. Golewski, Estimation of the optimum content of fly ash in concrete composite based on the analysis of fracture toughness tests using various measuring systems, Constr. Build. Mater. 213 (2019) 142–155, https://doi.org/10.1016/j.conbuildmat.2019.04.071.

[7] G.L. Golewski, Effect of curing time on the fracture toughness of fly ash concrete composites, Compos. Struct. 185 (2018) 105–112, https://doi.org/10.1016/j.compstruct.2017.10.090.

[8] G.L. Golewski, T. Sadowski, The fracture toughness the K IIIc of concretes with F fly ash (FA) additive, Constr. Build. Mater. 143 (2017) 444–454, https://doi.org/10.1016/j.conbuildmat.2017.03.137.

[9] G.L. Golewski, Measurement of fracture mechanics parameters of concrete containing fly ash thanks to use of Digital Image Correlation (DIC) method, Measurement 135 (2019) 96–105, https://doi.org/10.1016/j.measurement.2018.11.032.

[10] D. Hou, Y. Zhang, T. Yang, J. Zhang, H. Pei, J. Zhang, J. Jiang, T. Li, Molecular structure, dynamics, and mechanical behavior of sodium aluminosilicate hydrate (NASH) gel at elevated temperature: a molecular dynamics study, PCCP 20 (2018) 20695–20711.

[11] Y. Zhang, J. Zhang, J. Jiang, D. Hou, J. Zhang, The effect of water molecules on the structure, dynamics, and mechanical properties of sodium aluminosilicate hydrate (NASH) gel: A molecular dynamics study, Constr. Build. Mater. 193 (2018) 491–500.

[12] S. Das, A. Maroli, S.S. Singh, T. Stannard, X. Xiao, N. Chawla, N. Neithalath, A microstructure-guided constitutive modeling approach for random heterogeneous materials: Application to structural binders, Comput. Mater. Sci. 119 (2016) 52–64.

[13] X. Pardal, F. Brunet, T. Charpentier, I. Pochard, A. Nonat, 27Al and 29Si Solid-State NMR Characterization of Calcium-Aluminosilicate-Hydrate, Inorg. Chem. 51 (2012) 1827–1836, https://doi.org/10.1021/ic202124x.

[14] M. Bauchy, H. Laubie, M.J. Abdolhosseini Qomi, C.G. Hoover, F.-J. Ulm, R.-J.-M. Pellenq, Fracture toughness of calcium–silicate–hydrate from molecular dynamics simulations, J. Non-Cryst. Solids 419 (2015) 58–64.

[15] G. Geng, R.N. Vasin, J. Li, M.J.A. Qomi, J. Yan, H.-R. Wenk, P.J.M. Monteiro, Preferred orientation of calcium aluminosilicate hydrate induced by confined compression, Cem. Concr. Res. 113 (2018) 186–196, https://doi.org/10.1016/j.cemconres.2018.09.002.

[16] J. Němeček, V. Šmilauer, L. Kopecký, Nanoindentation characteristics of alkali-activated aluminosilicate materials, Cem. Concr. Compos. 33 (2011) 163–170, https://doi.org/10.1016/j.cemconcomp.2010.10.005.

[17] J.L. Provis, J.S.J. van Deventer, Geopolymers: Structures, Processing Properties and Industrial Applications, Elsevier, 2009.

[18] A. Fernandez-Jimenez, I. García-Lodeiro, A. Palomo, Durability of alkali-activated fly ash cementitious materials, J. Mater. Sci. 42 (2007) 3055–3065, https://doi.org/10.1007/s10853-006-0584-8.

[19] S. Wallah, B.V. Rangan, Low-Calcium fly ash-based geopolymer concrete: Long-term properties, 2006. https://espace.curtin.edu.au/handle/20.500.11937/34322 (accessed December 28, 2019).

[20] S. Das, P. Yang, S.S. Singh, J.C.E. Mertens, X. Xiao, N. Chawla, N. Neithalath, Effective properties of a fly ash geopolymer: Synergistic application of X-ray synchrotron tomography, nanoindentation, and homogenization models, Cem. Concr. Res. 78 (2015) 252–262.

[21] W.K.W. Lee, J.S.J. van Deventer, Use of Infrared Spectroscopy to Study Geopolymerization of Heterogeneous Amorphous Aluminosilicates, Langmuir 19 (2003) 8726–8734, https://doi.org/10.1021/la026127e.

[22] P. Duxson, J.L. Provis, G.C. Lukey, F. Separovic, J.S.J. van Deventer, 29Si NMR Study of Structural Ordering in Aluminosilicate Geopolymer Gels, Langmuir 21 (2005) 3028–3036.

[23] J.L. Provis, A. Hajimohammadi, C.E. White, S.A. Bernal, R.J. Myers, R.P. Winarski, V. Rose, T.E. Proffen, A. Llobet, J.S.J. van Deventer, Nanostructural characterization of geopolymers by advanced beamline techniques, Cem. Concr. Compos. 36 (2013) 56–64, https://doi.org/10.1016/j.cemconcomp.2012.07.003.

[24] C.E. White, J.L. Provis, A. Llobet, T. Proffen, J.S.J. van Deventer, Evolution of Local Structure in Geopolymer Gels: An *In Situ* Neutron Pair Distribution Function Analysis: Evolution of Local Structure in Geopolymer Gels, J. Am. Ceram. Soc. 94 (2011) 3532–3539.

[25] J.L. Provis, R.J. Myers, C.E. White, V. Rose, J.S.J. van Deventer, X-ray microtomography shows pore structure and tortuosity in alkali-activated binders, Cem. Concr. Res. 42 (2012) 855–864, https://doi.org/10.1016/j.cemconres.2012.03.004.

[26] C.E. White, J.L. Provis, T. Proffen, J.S.J. Van Deventer, The Effects of Temperature on the Local Structure of Metakaolin-Based Geopolymer Binder: A Neutron Pair Distribution Function Investigation: The Effects of Temperature on the Local Structure of Metakaolin-Based Geopolymer Binder, J. Am. Ceram. Soc. 93 (2010) 3486–3492.

[27] A. Autef, E. Joussein, G. Gasgnier, S. Rossignol, Role of the silica source on the geopolymerization rate: A thermal analysis study, J. Non-Cryst. Solids 366 (2013) 13–21, https://doi.org/10.1016/j.jnoncrysol.2013.01.034.

[28] F. Škvára, L. Kopecký, V. Šmilauer, Z. Bittnar, Material and structural characterization of alkali activated low-calcium brown coal fly ash, J. Hazard. Mater. 168 (2009) 711–720.

[29] J. Duchesne, L. Duong, T. Bostrom, R. Frost, Microstructure Study of Early In Situ Reaction of Fly Ash Geopolymer Observed by Environmental Scanning Electron Microscopy (ESEM), Waste Biomass Valor. 1 (2010) 367–377, https://doi.org/10.1007/s12649-010-9036-4.

[30] H. Lee, V. Vimonsatit, P. Chindaprasirt, Mechanical and micromechanical properties of alkali activated fly-ash cement based on nano-indentation, Constr. Build. Mater. 107 (2016) 95–102, https://doi.org/10.1016/j.conbuildmat.2015.12.013.

[31] J. Němeček, V. Šmilauer, L. Kopecký, Characterization of Alkali-Activated Fly-Ash by Nanoindentation, in: Z. Bittnar, P.J.M. Bartos, J. Němeček, V. Šmilauer, J. Zeman (Eds.), Nanotechnology in Construction 3, Springer, Berlin, Heidelberg, 2009, pp. 337–343, https://doi.org/10.1007/978-3-642-00980-8_45.

[32] C. Hu, Z. Li, A review on the mechanical properties of cement-based materials measured by nanoindentation, Constr. Build. Mater. 90 (2015) 80–90, https://doi.org/10.1016/j.conbuildmat.2015.05.008.

[33] Z. Luo, W. Li, Y. Gan, K. Mendu, S.P. Shah, Applying grid nanoindentation and maximum likelihood estimation for N-A-S-H gel in geopolymer paste: Investigation and discussion, Cem. Concr. Res. 135 (2020) 106112, https://doi.org/10.1016/j.cemconres.2020.106112.

[34] M. Ameri, S.h. Nowbakht, M. Molayem, M.R.M. Aliha, Investigation of fatigue and fracture properties of asphalt mixtures modified with carbon nanotubes: Fatigue and Fracture Properties of CNT-modified Asphalt Mixtures, Fatigue Frac.t Engng. Mater. Struct. 39 (2016) 896–906, https://doi.org/10.1111/ffe.12408.

[35] M. Ameri, A. Mansourian, S. Pirmohammad, M.R.M. Aliha, M.R. Ayatollahi, Mixed mode fracture resistance of asphalt concrete mixtures, Eng. Fract. Mech. 93 (2012) 153–167, https://doi.org/10.1016/j.engfracmech.2012.06.015.

[36] M.R.M. Aliha, H.R. Fattahi Amirdehi, Fracture toughness prediction using Weibull statistical method for asphalt mixtures containing different air void contents: Asphalt Fracture Toughness Prediction Using Weibull Statistical Method, Fatigue Fract. Engng. Mater Struct. 40 (2017) 55–68, https://doi.org/10.1111/ffe.12474.

[37] M.R.M. Aliha, H. Fazaeli, S. Aghajani, F. Moghadas Nejad, Effect of temperature and air void on mixed mode fracture toughness of modified asphalt mixtures, Constr. Build. Mater. 95 (2015) 545–555, https://doi.org/10.1016/j.conbuildmat.2015.07.165.
[38] M. Fakhri, E. Amoosoltani, M.R.M. Aliha, Crack behavior analysis of roller compacted concrete mixtures containing reclaimed asphalt pavement and crumb rubber, Eng. Fract. Mech. 180 (2017) 43–59, https://doi.org/10.1016/j.engfracmech.2017.05.011.
[39] M. Fakhri, E. Haghighat Kharrazi, M.R.M. Aliha, Mixed mode tensile – In plane shear fracture energy determination for hot mix asphalt mixtures under intermediate temperature conditions, Eng. Fract. Mechan. 192 (2018) 98–113. https://doi.org/10.1016/j.engfracmech.2018.02.007.
[40] H.R. Fattahi Amirdehi, M.R.M. Aliha, A. Moniri, A.R. Torabi, Using the generalized maximum tangential stress criterion to predict mode II fracture of hot mix asphalt in terms of mode I results – A statistical analysis, Constr. Build. Mater. 213 (2019) 483–491, https://doi.org/10.1016/j.conbuildmat.2019.04.067.
[41] M.R.M. Aliha, M. Fakhri, E. Haghighat Kharrazi, F. Berto, The effect of loading rate on fracture energy of asphalt mixture at intermediate temperatures and under different loading modes, Frattura Ed Integrità Strutturale. 12 (2017) 113–132, https://doi.org/10.3221/IGF-ESIS.43.09.
[42] P.J. Haghighat Pour, M.R.M. Aliha, M.R. Keymanesh, Evaluating mode I fracture resistance in asphalt mixtures using edge notched disc bend ENDB specimen with different geometrical and environmental conditions, Eng. Fract. Mechan. 190 (2018) 245–258. https://doi.org/10.1016/j.engfracmech.2017.11.007.
[43] H. Motamedi, H. Fazaeli, M.R.M. Aliha, H. Reza Amiri, Evaluation of temperature and loading rate effect on fracture toughness of fiber reinforced asphalt mixture using edge notched disc bend (ENDB) specimen, Constr. Build. Mater. 234 (2020) 117365, https://doi.org/10.1016/j.conbuildmat.2019.117365.
[44] M.R. Eghbali, M. Fallah Tafti, M.R.M. Aliha, H. Motamedi, The effect of ENDB specimen geometry on mode I fracture toughness and fracture energy of HMA and SMA mixtures at low temperatures, Eng. Fract. Mech. 216 (2019) 106496, https://doi.org/10.1016/j.engfracmech.2019.106496.
[45] S. Das, D. Stone, B. Mobasher, N. Neithalath, Strain energy and process zone based fracture characterization of a novel iron carbonate binding material, Eng. Fract. Mech. 156 (2016) 1–15.
[46] S. Das, A. Hendrix, D. Stone, N. Neithalath, Flexural fracture response of a novel iron carbonate matrix – Glass fiber composite and its comparison to Portland cement-based composites, Constr. Build. Mater. 93 (2015) 360–370.
[47] S. Das, M. Aguayo, G. Sant, B. Mobasher, N. Neithalath, Fracture process zone and tensile behavior of blended binders containing limestone powder, Cem. Concr. Res. 73 (2015) 51–62, https://doi.org/10.1016/j.cemconres.2015.03.002.
[48] S. Das, M. Aguayo, V. Dey, R. Kachala, B. Mobasher, G. Sant, N. Neithalath, The fracture response of blended formulations containing limestone powder: Evaluations using two-parameter fracture model and digital image correlation, Cem. Concr. Compos. 53 (2014) 316–326, https://doi.org/10.1016/j.cemconcomp.2014.07.018.
[49] A. Dakhane, S. Das, H. Hansen, S. O'Donnell, F. Hanoon, A. Rushton, c. Perla, N. Neithalath, Crack Healing in Cementitious Mortars Using Enzyme-Induced Carbonate Precipitation: Quantification Based on Fracture Response, J. Mater. Civ. Eng. 30 (2018) 04018035, https://doi.org/10.1061/(ASCE)MT.1943-5533.0002218.
[50] S. Das, M. Aguayo, N. Kabay, B. Mobasher, G. Sant, N. Neithalath, Elucidating the influences of compliant microscale inclusions on the fracture behavior of cementitious composites, Cem. Concr. Compos. 94 (2018) 13–23, https://doi.org/10.1016/j.cemconcomp.2018.08.009.
[51] S. Nayak, A. Kizilkanat, N. Neithalath, S. Das, Experimental and Numerical Investigation of the Fracture Behavior of Particle Reinforced Alkali Activated Slag Mortars, J. Mater. Civ. Eng. 31 (2019) 04019043.
[52] J. Moghal, A. Bird, A.H. Harris, B.D. Beake, M. Gardener, G. Wakefield, Nanomechanical study of thin film nanocomposite and PVD thin films on polymer substrates for optical applications, J. Phys. D: Appl. Phys. 46 (2013) 485303, https://doi.org/10.1088/0022-3727/46/48/485303.
[53] J. Chen, S.J. Bull, Indentation fracture and toughness assessment for thin optical coatings on glass, J. Phys. D: Appl. Phys. 40 (2007) 5401–5417, https://doi.org/10.1088/0022-3727/40/18/S01.
[54] Y.-T. Cheng, C.-M. Cheng, Relationships between hardness, elastic modulus, and the work of indentation, Appl. Phys. Lett. 73 (1998) 614–616, https://doi.org/10.1063/1.121873.
[55] J. Mencik, Micro-indentation tests with pointed indenters, Mater. Forum 18 (1994) 277.
[56] J. Chen, S.J. Bull, Modelling the limits of coating toughness in brittle coated systems, Thin Solid Films 517 (2009) 2945–2952, https://doi.org/10.1016/j.tsf.2008.12.054.
[57] J. Chen, S.J. Bull, Multi-cycling nanoindentation study on thin optical coatings on glass, J. Phys. D: Appl. Phys. 41 (2008) 074009, https://doi.org/10.1088/0022-3727/41/7/074009.
[58] Y. Liu, Fracture toughness assessment of shales by nanoindentation, University of Massachusetts-Amherst, Masters, 2015. https://scholarworks.umass.edu/cee_geotechnical/4.
[59] K. Liu, M. Ostadhassan, B. Bubach, Applications of nano-indentation methods to estimate nanoscale mechanical properties of shale reservoir rocks, J. Nat. Gas Sci. Eng. 35 (2016) 1310–1319, https://doi.org/10.1016/j.jngse.2016.09.068.
[60] Q. Zeng, Y. Wu, Y. Liu, G. Zhang, Determining the micro-fracture properties of Antrim gas shale by an improved micro-indentation method, J. Nat. Gas Sci. Eng. 62 (2019) 224–235, https://doi.org/10.1016/j.jngse.2018.12.013.
[61] D.S. Harding, W.C. Oliver, G.M. Pharr, Cracking During Nanoindentation and its Use in the Measurement of Fracture Toughness, MRS Online, Proceedings Library Archive. 356 (1994), https://doi.org/10.1557/PROC-356-663.
[62] M.R. Taha, E. Soliman, M. Sheyka, A. Reinhardt, M. Al-Haik, Fracture toughness of hydrated cement paste using nanoindentation, (2010) 7.
[63] J. Chen, S.J. Bull, Assessment of the toughness of thin coatings using nanoindentation under displacement control, Thin Solid Films 494 (2006) 1–7, https://doi.org/10.1016/j.tsf.2005.08.176.
[64] M.M.R. Taha, E. Soliman, M.P. Sheyka, A. Reinhardt, M. Al-Haik, Fracture toughness of hydrated cement paste using nanoindentation, in (2010).
[65] Aboubakr S. H., Soliman E. M., Taha M. M. Reda, Fracture Toughness of Synthetic C-S-H Using Nanoindentation, CONCREEP 10. (n.d.) 517–526. https://doi.org/10.1061/9780784479346.062.
[66] E.M. Soliman, S.H. Aboubakr, M.M. Reda Taha, Estimating fracture toughness of C-S–H using nanoindentation and the extended finite element method, Int. J. Adv. Eng. Sci. Appl. Math. 9 (2017) 154–168, https://doi.org/10.1007/s12572-017-0191-8.
[67] S. Xu, Y. Feng, J. Liu, Q. Zeng, Micro indentation fracture of cement paste assessed by energy-based method: The method improvement and affecting factors, Constr. Build. Mater. 231 (2020) 117136, https://doi.org/10.1016/j.conbuildmat.2019.117136.
[68] M.R. Sadat, S. Bringuier, K. Muralidharan, K. Runge, A. Asaduzzaman, L. Zhang, An atomistic characterization of the interplay between composition, structure and mechanical properties of amorphous geopolymer binders, J. Non-Cryst. Solids 434 (2016) 53–61.
[69] M.R. Sadat, S. Bringuier, K. Muralidharan, G. Frantziskonis, L. Zhang, Atomic-scale dynamics and mechanical response of geopolymer binder under nanoindentation, Comput. Mater. Sci. 142 (2018) 227–236.
[70] M.R. Sadat, S. Bringuier, A. Asaduzzaman, K. Muralidharan, L. Zhang, A molecular dynamics study of the role of molecular water on the structure and mechanics of amorphous geopolymer binders, J. Chem. Phys. 145 (2016) 134706.
[71] M. Zhang, N.A. Deskins, G. Zhang, R.T. Cygan, M. Tao, Modeling the Polymerization Process for Geopolymer Synthesis through Reactive Molecular Dynamics Simulations, J. Phys. Chem. C. 122 (2018) 6760–6773.
[72] G.A. Lyngdoh, R. Kumar, N.M.A. Krishnan, S. Das, Realistic atomic structure of fly ash-based geopolymer gels: Insights from molecular dynamics simulations, J. Chem. Phys. 151 (2019) 064307.
[73] F. Lolli, H. Manzano, J.L. Provis, M.C. Bignozzi, E. Masoero, Atomistic Simulations of Geopolymer Models: The Impact of Disorder on Structure and Mechanics, ACS Appl. Mater. Interfaces. 10 (2018) 22809–22820.
[74] F. Lolli, H. Manzano, J.L. Provis, M.C. Bignozzi, E. Masoero, Molecular model of geopolymers with increasing level of disorder in the atomic structure, International Conference on Alkali Activated Materials and Geopolymers: Versatile Materials Offering High Performance and Low Emissions. (2018). https://dc.engconfintl.org/geopolymers/97.
[75] J. Puibasset, R.-J.-M. Pellenq, Grand Canonical Monte Carlo Simulation Study of Water Adsorption in Silicalite at 300 K, J. Phys. Chem. B 112 (2008) 6390–6397.
[76] A.C.T. van Duin, S. Dasgupta, F. Lorant, W.A. Goddard, ReaxFF: A Reactive Force Field for Hydrocarbons, J. Phys. Chem. A. 105 (2001) 9396–9409.
[77] C09 Committee, Specification for Coal Fly Ash and Raw or Calcined Natural Pozzolan for Use in Concrete, ASTM International, n.d. https://doi.org/10.1520/C0618-19.
[78] D. Ravikumar, S. Peethamparan, N. Neithalath, Structure and strength of NaOH activated concretes containing fly ash or GGBFS as the sole binder, Cem. Concr. Compos. 32 (2010) 399–410.
[79] C01 Committee, Test Method for Compressive Strength of Hydraulic Cement Mortars (Using 2-in. or [50-mm] Cube Specimens), ASTM International, n.d. https://doi.org/10.1520/C0109_C0109M-16A.
[80] S. Das, D. Stone, D. Convey, N. Neithalath, Pore- and micro-structural characterization of a novel structural binder based on iron carbonation, Mater. Charact. 98 (2014) 168–179.
[81] R. Kumar, B. Bhattacharjee, Study on some factors affecting the results in the use of MIP method in concrete research, Cem. Concr. Res. 33 (2003) 417–424, https://doi.org/10.1016/S0008-8846(02)00974-2.
[82] H.Y. Moon, H.S. Kim, D.S. Choi, Relationship between average pore diameter and chloride diffusivity in various concretes, Constr. Build. Mater. 20 (2006) 725–732, https://doi.org/10.1016/j.conbuildmat.2005.02.005.
[83] E.J. Garboczi, D.P. Bentz, The effect of statistical fluctuation, finite size error, and digital resolution on the phase percolation and transport properties of the NIST cement hydration model, Cem. Concr. Res. 31 (2001) 1501–1514, https://doi.org/10.1016/S0008-8846(01)00593-2.
[84] F.-J. Ulm, M. Vandamme, C. Bobko, J.A. Ortega, K. Tai, C. Ortiz, Statistical Indentation Techniques for Hydrated Nanocomposites: Concrete, Bone, and Shale, J. Am. Ceram. Soc. 90 (2007) 2677–2692, https://doi.org/10.1111/j.1551-2916.2007.02012.x.
[85] L. Sorelli, G. Constantinides, F.-J. Ulm, F. Toutlemonde, The nano-mechanical signature of Ultra High Performance Concrete by statistical nanoindentation techniques, Cem. Concr. Res. 38 (2008) 1447–1456, https://doi.org/10.1016/j.cemconres.2008.09.002.

[86] J.H. Lee, Y.F. Gao, K.E. Johanns, G.M. Pharr, Cohesive interface simulations of indentation cracking as a fracture toughness measurement method for brittle materials, Acta Mater. 60 (2012) 5448–5467, https://doi.org/10.1016/j.actamat.2012.07.011.
[87] K.E. Johanns, J.H. Lee, Y.F. Gao, G.M. Pharr, An evaluation of the advantages and limitations in simulating indentation cracking with cohesive zone finite elements, Modelling Simul. Mater. Sci. Eng. 22 (2013) 015011, https://doi.org/10.1088/0965-0393/22/1/015011.
[88] D.J. Morris, R.F. Cook, Indentation fracture of low-dielectric constant films: Part II. Indentation fracture mechanics model, J. Mater. Res. 23 (2008) 2443–2457, https://doi.org/10.1557/jmr.2008.0295.
[89] M. Sebastiani, K.E. Johanns, E.G. Herbert, G.M. Pharr, Measurement of fracture toughness by nanoindentation methods: Recent advances and future challenges, Curr. Opin. Solid State Mater. Sci. 19 (2015) 324–333.
[90] A. Moradkhani, H. Baharvandi, M. Tajdari, H. Latifi, J. Martikainen, Determination of fracture toughness using the area of micro-crack tracks left in brittle materials by Vickers indentation test, J. Adv. Ceram. 2 (2013) 87–102, https://doi.org/10.1007/s40145-013-0047-z.
[91] T. Bakharev, Geopolymeric materials prepared using Class F fly ash and elevated temperature curing, Cem. Concr. Res. 35 (2005) 1224–1232.
[92] J.S.J. van Deventer, J.L. Provis, P. Duxson, G.C. Lukey, Reaction mechanisms in the geopolymeric conversion of inorganic waste to useful products, J. Hazard. Mater. 139 (2007) 506–513.
[93] W.c. Oliver, G.m. Pharr, Measurement of hardness and elastic modulus by instrumented indentation: Advances in understanding and refinements to methodology, J. Mater. Res. 19 (2004) 3–20, https://doi.org/10.1557/jmr.2004.19.1.3.
[94] X. Li, B. Bhushan, A review of nanoindentation continuous stiffness measurement technique and its applications, Mater. Charact. 48 (2002) 11–36, https://doi.org/10.1016/S1044-5803(02)00192-4.
[95] N.R. Moody, W.W. Gerberich, N. Burnham, S.P. Baker, Fundamentals of nanoindentation and nanotribology, Warrendale, PA (United States); Mater. Res. Soc. 1998. http://www.osti.gov/scitech/biblio/6177899 (accessed February 25, 2015).
[96] W.c. Oliver, G.m. Pharr, An improved technique for determining hardness and elastic modulus using load and displacement sensing indentation experiments, J. Mater. Res. 7 (1992) 1564–1583, https://doi.org/10.1557/JMR.1992.1564.
[97] W.R.L. da Silva, J. Němeček, P. Štemberk, Application of multiscale elastic homogenization based on nanoindentation for high performance concrete, Adv. Eng. Softw. 62–63 (2013) 109–118, https://doi.org/10.1016/j.advengsoft.2013.04.007.
[98] J. Němeček, V. Králík, J. Vondřejc, Micromechanical analysis of heterogeneous structural materials, Cem. Concr. Compos. 36 (2013) 85–92.
[99] I. Beleña, W. Zhu, Nanoindentation Study of Na-Geopolymers Exposed to High Temperatures, in: Z. Bittnar, P.J.M. Bartos, J. Němeček, V. Šmilauer, J. Zeman (Eds.), Nanotechnology in Construction 3, Springer, Berlin, Heidelberg, 2009, pp. 169–174, https://doi.org/10.1007/978-3-642-00980-8_22.
[100] B. Lawn, R. Wilshaw, Indentation fracture: principles and applications, J. Mater. Sci. 10 (1975) 1049–1081, https://doi.org/10.1007/BF00823224.
[101] B.R. Lawn, B.J. Hockey, S.M. Wiederhorn, Atomically sharp cracks in brittle solids: an electron microscopy study, J. Mater. Sci. 15 (1980) 1207–1223.
[102] G.R. Anstis, P. Chantikul, B.R. Lawn, D.B. Marshall, A Critical Evaluation of Indentation Techniques for Measuring Fracture Toughness: I, Direct Crack Measurements, J. Am. Ceram. Soc. 64 (1981) 533–538, https://doi.org/10.1111/j.1151-2916.1981.tb10320.x.
[103] P. Chantikul, G.R. Anstis, B.R. Lawn, D.B. Marshall, A Critical Evaluation of Indentation Techniques for Measuring Fracture Toughness: II, Strength Method, J. Am. Ceram. Soc. 64 (1981) 539–543, https://doi.org/10.1111/j.1151-2916.1981.tb10321.x.
[104] T. Phoo-ngernkham, V. Sata, S. Hanjitsuwan, C. Ridtirud, S. Hatanaka, P. Chindaprasirt, Compressive strength, Bending and Fracture Characteristics of High Calcium Fly Ash Geopolymer Mortar Containing Portland Cement Cured at Ambient Temperature, Arab. J. Sci. Eng. 41 (2016) 1263–1271, https://doi.org/10.1007/s13369-015-1906-4.
[105] P. Rovnaník, H. Šimonová, L. Topolář, P. Schmid, Z. Keršner, Effect of Carbon Nanotubes on the Mechanical Fracture Properties of Fly Ash Geopolymer, Procedia Eng. 151 (2016) 321–328, https://doi.org/10.1016/j.proeng.2016.07.360.
[106] P.K. Sarker, R. Haque, K.V. Ramgolam, Fracture behaviour of heat cured fly ash based geopolymer concrete, Mater. Des. 44 (2013) 580–586, https://doi.org/10.1016/j.matdes.2012.08.005.
[107] X. Li, W. Song, K. Yang, N.M.A. Krishnan, B. Wang, M.M. Smedskjaer, J.C. Mauro, G. Sant, M. Balonis, M. Bauchy, Cooling rate effects in sodium silicate glasses: Bridging the gap between molecular dynamics simulations and experiments, J. Chem. Phys. 147 (2017) 074501.
[108] N.P. Bansal, R.H. Doremus, Handbook of Glass Properties, Academic Press, 1986.
[109] I. Simon, Structure of Neutron-Irradiated Quartz and Vitreous Silica, J. Am. Ceram. Soc. 40 (1957) 150–153, https://doi.org/10.1111/j.1151-2916.1957.tb12593.x.
[110] R.J.-M. Pellenq, A. Kushima, R. Shahsavari, K.J. Van Vliet, M.J. Buehler, S. Yip, F.-J. Ulm, A realistic molecular model of cement hydrates, Proc. Natl. Acad. Sci. 106 (2009) 16102–16107.
[111] N.M.A. Krishnan, B. Wang, G. Falzone, Y. Le Pape, N. Neithalath, L. Pilon, M. Bauchy, G. Sant, Confined Water in Layered Silicates: The Origin of Anomalous Thermal Expansion Behavior in Calcium-Silicate-Hydrates, ACS Appl. Mater. Interfaces. 8 (2016) 35621–35627.
[112] H.M. Aktulga, J.C. Fogarty, S.A. Pandit, A.Y. Grama, Parallel reactive molecular dynamics: Numerical methods and algorithmic techniques, Parallel Comput. 38 (2012) 245–259.
[113] D. Frenkel, B. Smit, Understanding Molecular Simulation: From Algorithms to Applications, Elsevier, 2001.
[114] W.G. Hoover, Canonical dynamics: Equilibrium phase-space distributions, Phys. Rev. A. 31 (1985) 1695–1697.
[115] S. Nosé, A molecular dynamics method for simulations in the canonical ensemble, Mol. Phys. 52 (1984) 255–268.
[116] S. Plimpton, Fast Parallel Algorithms for Short-Range Molecular Dynamics, J. Comput. Phys. 117 (1995) 1–19.
[117] L. Ly, E.R. Vance, D.S. Perera, Z. Aly, K. Olufson, Leaching of Geopolymers in Deionised Water, Adv. Technol. Mater. Mater. Process. J. 8 (2006) 236–247.
[118] P. Duxson, G.C. Lukey, J.S.J. van Deventer, Physical evolution of Na-geopolymer derived from metakaolin up to 1000 °C, J. Mater. Sci. 42 (2007) 3044–3054.
[119] L. Cormier, D. Ghaleb, D.R. Neuville, J.-M. Delaye, G. Calas, Chemical dependence of network topology of calcium aluminosilicate glasses: a computer simulation study, J. Non-Cryst. Solids 332 (2003) 255–270.
[120] N.M.A. Krishnan, B. Wang, Y. Le Pape, G. Sant, M. Bauchy, Irradiation-driven amorphous-to-glassy transition in quartz: The crucial role of the medium-range order in crystallization, Phys. Rev. Mater. 1 (2017).
[121] M. Bauchy, Structural, vibrational, and elastic properties of a calcium aluminosilicate glass from molecular dynamics simulations: The role of the potential, J. Chem. Phys. 141 (2014) 024507.
[122] A.C. Wright, The comparison of molecular dynamics simulations with diffraction experiments, J. Non-Cryst. Solids 159 (1993) 264–268.
[123] Y. Yu, B. Wang, Y.J. Lee, M. Bauchy, Fracture Toughness of Silicate Glasses: Insights from Molecular Dynamics Simulations, MRS Proceedings. 1757 (2015) mrsf14-1757-uu09-02.
[124] Brochard Laurent, Hantal Gyorgy, Laubie Hadrien, Ulm Franz J., Pellenq Roland J. -M., Fracture Mechanisms in Organic-Rich Shales: Role of Kerogen, Poromechanics V. (n.d.) 2471–2480.
[125] R. Ravinder, A. Kumar, R. Kumar, P. Vangla, N.M.A. Krishnan, Irradiation-induced brittle-to-ductile transition in α-quartz, J Am Ceram Soc. (2019) 1–9, https://doi.org/10.1111/jace.16951.
[126] L. Brochard, G. Hantal, H. Laubie, F.-J. Ulm, R.J.M. Pellenq, Capturing material toughness by molecular simulation: accounting for large yielding effects and limits, Int. J. Fract. 194 (2015) 149–167.
[127] S.C. Chowdhury, B.Z. (Gama) Haque, J.W. Gillespie, Molecular dynamics simulations of the structure and mechanical properties of silica glass using ReaxFF, J. Mater. Sci. 51 (2016) 10139–10159, https://doi.org/10.1007/s10853-016-0242-8.
[128] D. Hou, J. Zhang, Z. Li, Y. Zhu, Uniaxial tension study of calcium silicate hydrate (C–S–H): structure, dynamics and mechanical properties, Mater Struct. 48 (2015) 3811–3824.
[129] Griffith Alan Arnold, Taylor Geoffrey Ingram, VI. The phenomena of rupture and flow in solids, Philosophical Transactions of the Royal Society of London. Series A, Containing Papers of a Mathematical or Physical Character. 221 (1921) 163–198.
[130] J.-B. Leblond, Rupture fragile et rupture ductile, Comptes Rendus de l'Académie Des Sciences - Series IIB - Mechanics-Physics-Chemistry-Astronomy. 326 (1998) 243–250.
[131] T.L. Anderson, Fracture Mechanics: Fundamentals and Applications, CRC Press/Taylor & Francis (2005).
[132] B. Wang, Y. Yu, Y.J. Lee, M. Bauchy, Intrinsic Nano-Ductility of Glasses: The Critical Role of Composition, Front. Mater. 2 (2015).
[133] G.I. Barenblatt, The Mathematical Theory of Equilibrium Cracks in Brittle Fracture, in: H.L. Dryden, Th. von Kármán, G. Kuerti, F.H. van den Dungen, L. Howarth (Eds.), Advances in Applied Mechanics, Elsevier, 1962, pp. 55–129, https://doi.org/10.1016/S0065-2156(08)70121-2.
[134] J.M. Lemm, Advances in Applied Mechanics, in, Academic Press, New York, 1962.
[135] D.S. Dugdale, Yielding of steel sheets containing slits, J. Mech. Phys. Solids 8 (1960) 100–104.
[136] G.R. Irwin, Fracture, in: S. Flügge (Ed.), Elasticity and Plasticity / Elastizität Und Plastizität, Springer Berlin Heidelberg, Berlin, Heidelberg, 1958: pp. 551–590. https://doi.org/10.1007/978-3-642-45887-3_5.